

## Article

# Shadow-imaging-based multiple sensing approach for tool deflection measurement

Marina Terlau <sup>1,\*</sup>, Axel von Freyberg <sup>1</sup>, Dirk Stöbener <sup>1,2</sup> and Andreas Fischer <sup>1,2</sup>

<sup>1</sup> University of Bremen, Bremen Institute for Metrology, Automation and Quality Science, Linzer Straße 13, D-28359 Bremen, Germany

<sup>2</sup> MAPEX Center for Materials and Processes, University of Bremen, P.O. box 330440, D-28334 Bremen, Germany

\* Correspondence: m.terlau@bimaq.de

**Abstract:** As incrementally formed sheets show large geometric deviations resulting from the deflection of the forming tool, an in-process measurement of the tool tip position is required. In order to cover a measuring volume of  $2.0\text{ m} \times 1.0\text{ m} \times 0.2\text{ m}$  and to achieve measuring uncertainties of less than  $50\text{ }\mu\text{m}$ , a multiple sensing approach is pursued. Each shadow imaging sensor in the multi-sensor system evaluates the direction vector to an LED attached to the tool, and the three-dimensional position of the LED is then determined from the combination of at least two sensors. Experimental results show that the angle of view from the sensor to the LED limits both the measurement range and the measurement uncertainty. The measurement uncertainty is dominated by systematic deviations, but these can be compensated, so that the measurement uncertainty required for measuring the tool tip position in the ISF is achieved.

**Keywords:** incremental sheet forming; multiple sensing; shadow imaging; three-dimensional position measurement

## 1. Introduction

### 1.1. Motivation

In comparison to conventional forming processes, incremental sheet forming (ISF) is an economical alternative for forming large sheet metals in small lot sizes [1]. Since a universally applicable forming stylus forms the sheet metal over a counter die with arbitrary shape [2], the machine tool costs are significantly reduced. However, one disadvantage of ISF is that major geometrical deviations occur due to spring back [3] and tool deflection [4]. To enable a compensation of the tool deflection, it must be determined. For this purpose, a prediction of the tool deflection using mechanical calculations is performed [5]. However, these predictions are based on model assumptions and do not consider the machine tool error or deformations of the machine tool. Therefore, a tool deflection measurement is preferred instead.

The required tool deflection measurement system must be capable of measuring the three-dimensional tool tip position in the ISF process. So, the measurement system has to work contact-less and fast, capturing the tool position close to the tool tip in a single shot. Additionally, the measurement system shall be independent of the machine tool kinematics.

### 1.2. State of the art

To meet the requirements for an in-process deflection measurement of the moving tool, optical measurement systems are reasonable approaches. In the intended application, a machining volume of  $2.0\text{ m} \times 1.0\text{ m} \times 0.2\text{ m}$  shall be covered by the measurement system. To enable the detection of typically occurring tool deflection of  $150\text{ }\mu\text{m} - 450\text{ }\mu\text{m}$  a measurement uncertainty of  $\leq 50\text{ }\mu\text{m}$  is targeted. Consequently, a challenging dynamic range (i.e. measurement range divided by measurement uncertainty) of  $4 \cdot 10^4$  is required.

**Citation:** Terlau, M.; von Freyberg, A.; Stöbener, D.; Fischer, A. Shadow-imaging-based multiple sensing approach for tool deflection measurement. *Sensors* **2023**, *1*, 0. <https://doi.org/>

Received:

Revised:

Accepted:

Published:

**Copyright:** © 2023 by the authors. Submitted to *Sensors* for possible open access publication under the terms and conditions of the Creative Commons Attribution (CC BY) license (<https://creativecommons.org/licenses/by/4.0/>).

Covering the entire measuring volume with a global measurement approach, e.g. full-field photogrammetry, the dynamic range is not achievable [6]. On the contrary, a local measurement approach, e.g. tracking laser interferometry, is capable of achieving the required dynamic range. Therefore, laser trackers are usually applied to measure the machine tool error [7]. Even in robotic ISF, a laser tracker has been applied to measure the tool center position in order to control the forming process in real time [8]. However, to determine the tool deflection and the machine deformation, a reflector must be attached close to the tool tip. The tracked reflector at the tool tip might move out of the system's field of view during a loss of view and then the tracking system fails. As a compromise between the local and the global measurement approach without scanning, a multiple sensing approach is proposed, where several sensors are arranged around the measuring volume and each sensor covers a small sub-region of the full volume [9]. Applying the multiple sensing approach, a setup that is robust to a loss of view is realizable and an enhanced dynamic range is achievable.

Since the sensors must be located outside the machining volume, an applicable sensor technology has to cover a sub-region of an axial measuring range of 500 mm, which is half the width of the machining volume. Additionally, a lateral measuring range in horizontal and vertical direction of 200 mm is aimed. Considering the time resolution, a measurement duration below 1 ms is required to keep motion blur sufficiently low when operating at a common feed rate of 50 mm/s [10]. For this purpose, the position has to be captured in a single shot. To provide a new position measurement at each 1 mm tool movement, a measuring rate of 50 Hz is necessary. Resulting from these requirements, camera-based methods determining a position by triangulation with an angle-of-view measurement are suitable, because they provide an appropriate field of view and exposure times below 1 ms, and frame rates above 50 Hz are feasible.

Photogrammetry is a particularly suitable approach for measuring the 3D positions of multiple points with reflector targets [11]. Industrial applications include deformation measurements, i.e. displacement field measurements of the object's surface, of a model in a wind tunnel [12] or a wind turbine blade in static and fatigue tests [13], alignment of row parts before machining [14] or tracking of robot end-effectors [15]. Although tracking robot end-effectors is a similar application to tool tip measurement, transferring the measurement principle is neither practical due to the use of reflector targets that are too large to be placed close to the tool tip, nor does it reach a sufficient dynamic range [6]. For photogrammetric shape measurement, artificial patterns are pasted on the surface of the measuring object [11]. Here, the 3D shape is obtained using stereoscopic digital image correlation (DIC). 3D DIC was applied, for example, for the analysis of 3D displacement fields in fracture experiments [16] or in ISF for measuring the shape of the formed part to iteratively control the forming process [17]. Siebert et al. [18] have shown that 3D DIC enables a sufficient dynamic range in lateral but not in axial direction with respect to the intended application in tool deflection measurement. Another approach to measure 3D displacement fields using only a single camera is based on laser speckles. Using speckle photography, Tausendfreund et al. [19] measured 3D displacement fields during the deep rolling process. To achieve a high spatial resolution, the field of view of the camera is less than 10 mm wide, which is a too small measurement range to cover a sufficient part of the machining volume in ISF. Therefore, due to the larger field of view, photogrammetric approaches seem more suitable for measuring the tool tip position in ISF. However, photogrammetric measurement is based on tracking markers on the object surface, i.e. the tool tip surface. As a result, the information is only contained in a few of more than a million pixels in the image.

In order to maximize the image information content and to use the full image frame of the camera, Grenet et al. introduced a shadow imaging concept to measure the position of a light source [20]. In shadow imaging, the light source casts a shadow through a mask in front of a camera chip and the light source position is calculated from the image of the shadow. Thereby, the lateral position is obtained from the shadow position and the axial position can either be calculated from the magnification of the shadow pattern or

from triangulating shadow positions of at least two sensors. To enable an absolute three-dimensional light source position measurement, i. e. an absolute two-dimensional shadow position evaluation, a checkerboard pattern with absolute coding or a center feature is proposed. Another pattern with absolute and two-dimensional features has been created by André et al. [21], which contains periodic arranged squares and binary absolute coding. The pattern is applied as micro-encoded target and the target's in-plane position is measured.

In summary, it stands out that stereo- and multi-camera systems, which are robust to failure, have not been used for measuring the tool tip position in ISF yet. Since the measurement uncertainty decreases with an increasing feature content in the image [22], the shadow imaging principle is pursued here for the application in ISF. Previous work has shown that shadow imaging is capable of achieving the required tool tip position measurement uncertainty of the lateral position components, but also that the required dynamic range of the axial position component is not achievable using a single shadow imaging sensor [23]. To increase the aperture and thus reduce the measurement uncertainty of the axial position component, the concept of using two shadow imaging sensors with overlapping measurement regions for the tool tip position measurement is proposed. However, it is unclear yet which combination of multiple shadow image sensors enables the 3D position measurement in the ISF machining volume. To solve this issue, the question arises which uncertainty is achieved in which measuring volume when the measuring regions of two sensors overlap. Additionally, the limits of the measurement range that one sensor can cover and the different contributions to the measurement uncertainty budget including the sensor calibration must be explored.

### 1.3. Aim and outline

The aim of the present article is to propose a multiple sensing approach based on shadow imaging sensors for measuring the 3D tool deflection in incremental sheet forming. Thereby, the measurement regions of two sensors overlap and the 3D tool tip position is measured by triangulation. On the one hand, the 3D measuring volume that two sensors are capable to cover is identified. On the other hand, the achievable measurement uncertainty of the three-dimensional tool tip position is assessed. The measurement uncertainty results from optical and geometrical influences, which also affect the calibration. To reveal further optimization potential, effects of these influences are investigated.

In the following, the 3D tool deflection measuring principle by means of a light emitting diode as point light source and two or more shadow imaging sensors is introduced in section 2. Section 3 presents the experimental setup that is subsequently used to investigate the dynamic range of a two-sensor system. Studying the achievable measurement range and the measurement uncertainty, respective experimental results are shown and discussed in section 4. Finally, section 5 gives a conclusion and an outlook.

## 2. Principle of measurement

To apply the shadow imaging principle for tool deflection measurement in ISF, a point light source is attached on the tool tip. For the determination of the light source position  $\mathbf{l} = (x_L, y_L, z_L)^T$ , two or more shadow imaging sensors are used, each of which consists of a mask and a camera chip. The light source casts a shadow through the mask on the camera chip. By evaluating the shadow position on the camera chip in the image, each sensor measures the direction to the light source. This means, each sensor  $n = 1, \dots, N$  provides possible light source positions  $\mathbf{l}'_n = (x'_{L,n}, y'_{L,n}, z'_{L,n})^T$  that are arranged in a line:

$$\mathbf{l}'_n = \mathbf{s}_n + t \cdot \mathbf{r}_{m,n}. \quad (1)$$

This line is defined by the sensor's position  $\mathbf{s}_n = (x_{s,n}, y_{s,n}, z_{s,n})^T$ , which is known from a calibration, and the measured direction vector  $\mathbf{r}_{m,n} = (r_{x,n}, r_{y,n}, r_{z,n})^T$  in the  $(x, y, z)$  machine coordinate system. The scalar parameter  $t$  leads to a certain point on the line. In practical 3D measurements, the lines measured by  $N$  sensors probably do not intersect, see

Fig. 1. Therefore, the best estimate  $\hat{l}$  of the sought light source position finally follows from the point with the closest squared distances  $d_n$  to all lines, i.e. by calculating

$$\min_{\hat{l}} \left( \sum_{n=1}^N (d_n(\hat{l}))^2 \right) \quad (2)$$

with

$$d_n(\hat{l}) = \frac{|(\hat{l} - s_n) \times r_{m,n}|}{|r_{m,n}|}. \quad (3)$$

As a result, for measuring the 3D light source position, it is necessary to determine the sensor positions  $s_n$  by calibration and to extract the direction vectors  $r_{m,n}$  from two or more sensors to the light source.

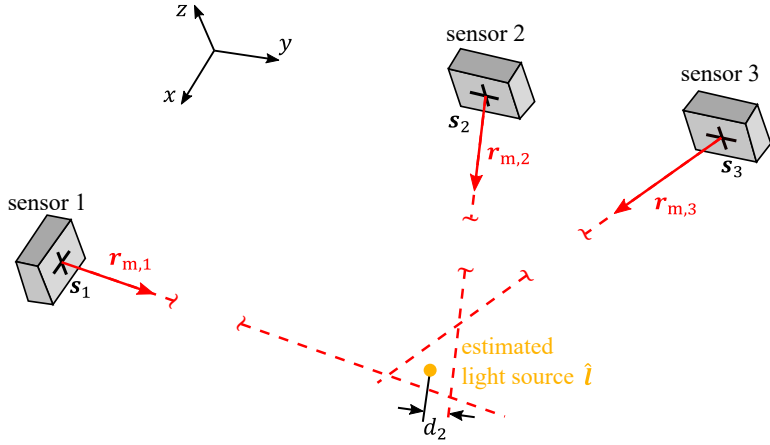


**Figure 1.** Principle of measuring the light source position by two or more (here three) sensors. The best estimate of the light source position  $\hat{l}$  is the point with the closest squared distances  $d_n$  to the red dashed lines, each of which is given by one sensor and contains possible light source positions. The distance  $d_2$  between sensor  $n = 2$  and the estimated light source position is exemplarily shown. Each sensor  $n = 1, \dots, N$  provides one line that is determined by the sensor's position  $s_n$  marked by a black cross and the evaluated direction vector  $r_{m,n}$  in the  $(x, y, z)$  machine coordinate system.

For the detailed explanation how the direction vectors are obtained, only one sensor is considered, and the index  $n$  specifying the sensor number is omitted in the following. The direction vector  $r_m$  in machine coordinates is obtained by a coordinate transformation of the direction vector  $r_s = (r_\xi, r_\eta, r_\zeta)^T$  that is detected in the  $(\xi, \eta, \zeta)$  sensor coordinate system. The coordinate transformation is a rotation by the angle  $\gamma$  around the  $z$ -axis, then by the angle  $\beta$  around the  $y$ -axis and lastly by the angle  $\alpha$  around the  $x$ -axis:

$$r_m = R_\alpha \cdot R_\beta \cdot R_\gamma \cdot r_s, \quad (4)$$

i.e. the elementary rotation matrices  $R_\alpha$ ,  $R_\beta$  and  $R_\gamma$  based on the respective rotation angles  $\alpha$ ,  $\beta$  and  $\gamma$ , which are obtained from the sensor calibration, are applied. The direction vector in sensor coordinates is

$$r_s = \begin{bmatrix} \tan(\Theta_s) \\ 1 \\ \tan(\Phi_s) \end{bmatrix} \quad (5)$$

and is based on the angles

$$\Theta_s = \arctan\left(\frac{\xi_{i,0} - \xi_i}{h}\right) \quad (6)$$

and

$$\Phi_s = \arctan\left(\frac{\zeta_{i,0} - \zeta_i}{h}\right) \quad (7)$$

that result from the shadow position  $(\xi_i, \zeta_i)$  detected in the camera image and calibrated intrinsic sensor parameters, namely the shadow position  $(\xi_{i,0}, \zeta_{i,0})$  when the light source is centered in front of the sensor and the distance  $h$  between mask and sensor. The relation between the shadow position  $(\xi_i, \zeta_i)$  and the direction vector  $\mathbf{r}_s = (r_\xi, r_\eta, r_\zeta)^\top$  in sensor coordinates including the sensor calibration parameters is visualized in Fig. 2. As a result of Eq. (4) to (7), each shadow imaging sensor finally provides the direction to the light source in machine coordinates. The position of the light source attached to the tool tip is then determined with the sensors' output and the calibrated sensors' positions by applying Eq. (2) and (3).

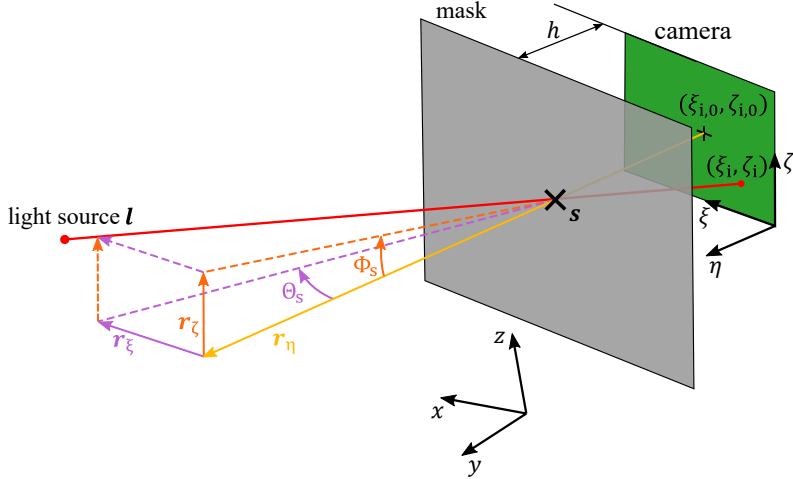


**Figure 2.** Principle of a single shadow imaging sensor. The light source at position  $l$  projects the shadow of a mask onto a camera chip. The shadow position  $(\xi_i, \zeta_i)$  is the position in the  $(\xi, \zeta)$  image plane where the shadow of the mask center, i. e. the sensor position  $s$  highlighted by a black cross, appears. The direction vector  $\mathbf{r}_s$  in sensor coordinates shown by its components  $r_\xi$ ,  $r_\eta$  and  $r_\zeta$  points to the light source.

### 3. Methods

#### 3.1. Shadow imaging sensor

For the experimental investigation of the 3D position measurement capability, a minimal setup with a light source and three shadow imaging sensors is used, see Fig. 3. Thereby, three sensors are applied to investigate the required measuring volume of one sensor. The light source, whose position is to be measured, is a surface-mounted device LED with a peak wavelength of 520 nm, a maximum luminous intensity of 1300 mcd and a beam angle of 140°. Each sensor consists of a 30 mm × 40 mm large mask with transparent and opaque parts, which is manufactured by laser exposure of a polyester film, and a DMM 37UX273-ML monochrome board camera from the company The Imaging Source. The camera has a resolution of 1440 px × 1080 px with a pixel size of 3.45 μm. The distance  $h$  between mask and camera is 20 mm.

##### 3.1.1. Mask

For measuring the absolute 3D position of the tool tip, i. e. the LED, a mask is required that contains features in horizontal and vertical direction and absolute features. A section of the used mask is shown in Fig. 4. The mask contains alternately arranged grids with vertical and horizontal stripes. Vertical stripes enable to determine the horizontal shadow position  $\xi_i$  and horizontal stripes allow the evaluation of the vertical shadow position  $\zeta_i$ , respectively. In order to ensure that at least one full grid is always visible in the image while the LED is moved through the entire measurement volume, each grid has a size of 2.0 mm × 1.5 mm. Each stripe in a grid is 100 μm wide. The absolute feature is realized by 8-bit binary codes in each first transparent stripe of a grid. Eight adjacent squares are either

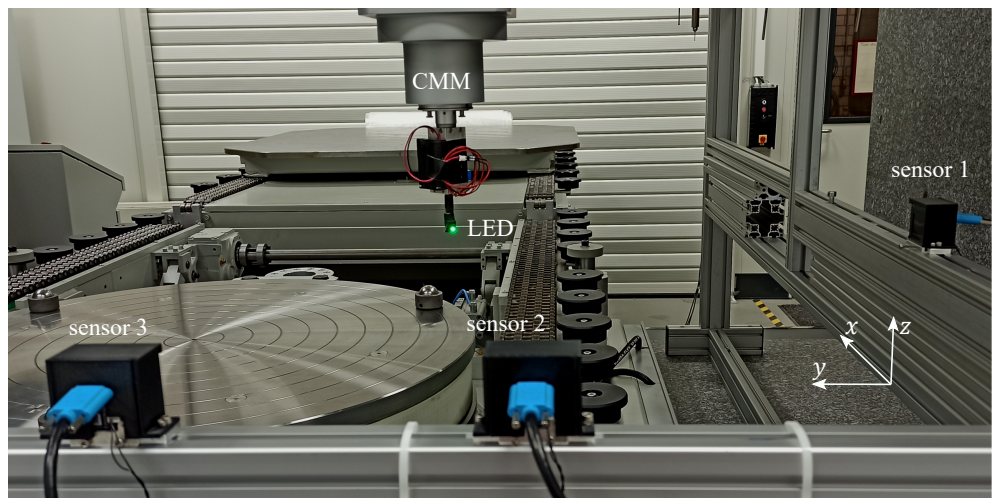


**Figure 3.** Experimental setup to investigate the 3D position measurement capability of a measurement system of several shadow imaging sensors in a measurement volume of 500 mm × 300 mm × 200 mm. The LED is positioned by a coordinate measuring machine (CMM), which also serves as reference system.

transparent and provide a '0' or opaque and provide a '1' and so form an index of the grid. In the mask, each index is used twice, once for a vertical grid and once for a horizontal grid. The index defines where each grid is located with respect to the mask center. Therefore, the coded grid mask enables to determine the absolute shadow position of the mask center in horizontal and vertical direction so that the absolute 3D LED position can be measured by two or more sensors.

### 3.1.2. Image processing

To determine the position, where the shadow of the mask center occurs in the image plane, the grids must be segmented first. In a second step, the stripes in each grid are localized, and then, the index is read in the binary coded stripe. The position of the shadow of the mask center is then obtained by evaluating the location of the shadows of the stripes visible in the image, the location of these stripes in the mask with respect to the mask center and the magnification of the stripe spacing in the shadow image with respect to the stripe spacing in the mask.

To separate the grids, the detection of horizontal and vertical borders is necessary. For visualization, an example image with evaluated intensity profiles is shown in Fig. 5. Horizontal borders are located as the drop of the intensity after a bright vertical stripe. A vertical stripe is detected as a peak in the column-wise averaged intensity. A previously performed low-pass-filtering ensures robustness of the image processing against noise. Then, the horizontal borders are located in the row, where the filtered column intensity first passes through a threshold intensity after a plateau on a higher level. Thereby, the threshold intensity is the average intensity of the entire image and the intensity plateau indicates a stripe of a vertical grid. A respective intensity profile is given by the orange profile in Fig. 5. Similarly, vertical borders are detected. A right border of a horizontal grid is where the filtered intensity passes through a threshold on the right side of the high-level-plateau, i.e. a horizontal bright stripe in the image, see the blue intensity profile in Fig. 5. Accordingly, the left border of a horizontal grid is where the intensity passes through the threshold on the left side of a low-level-plateau, i.e. a dark horizontal stripe, as shown by the intensity profile in Fig. 5.

In each grid, the stripes are localized by approximating a model function because preliminary investigations have shown that this method provides more accurate results than a phase evaluation or a correlation [24]. Before the approximation, the image section

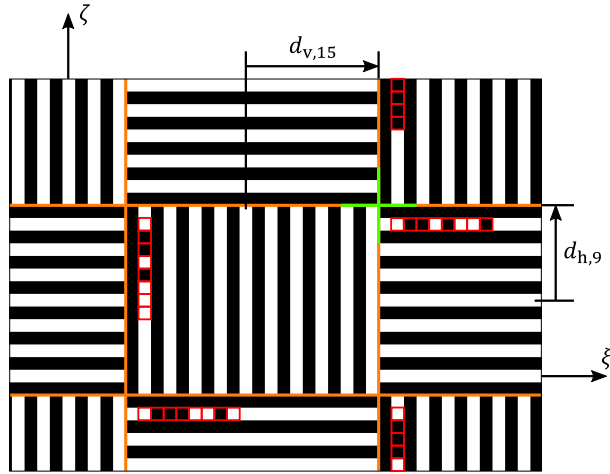


**Figure 4.** Section of the mask used in the shadow imaging sensors. The mask is the black and white structure wherein black areas represent opaque contents and white areas transparent contents. The orange lines highlight the borders between the horizontal and vertical grids. The red squares visualize the bits used to build the binary index of each grid. The center of the entire mask is marked by the green cross. The axes  $\xi$  and  $\zeta$  are projected from the sensor coordinate system to the mask plane. The distances  $d_{v,a}$  and  $d_{h,b}$  in the mask plane between the mask center and the stripes with the number  $a$  and  $b$  respectively are known. As an example, the distances  $d_{v,a}$  and  $d_{h,b}$  for the stripes  $a = 15$  and  $b = 9$  are visualized.

is averaged in the direction of the stripes and a low-pass-filter is applied to smoothen interferences due to noise and diffraction. Then, the intensity profile of a vertical bright stripe  $a$  in the region between adjacent intensity minima is approximated by the model function

$$I_{M,v}(\xi) = \begin{cases} I'_{M,v}(\xi) & \text{for } I'_{M,v}(\xi) < I_{\max,v,a} \\ I_{\max,v,a} & \text{for } I'_{M,v}(\xi) \geq I_{\max,v,a} \end{cases} \quad (8)$$

with

$$I'_{M,v}(\xi) = I_{0,v,a} + A_{v,a} \cdot e^{-\left(\frac{|\xi-\mu_{v,a}|}{w_{v,a}}\right)^2}$$

and the intensity profile of each horizontal bright stripe  $b$  is approximated by the model function

$$I_{M,h}(\zeta) = \begin{cases} I'_{M,h}(\zeta) & \text{for } I'_{M,h}(\zeta) < I_{\max,h,b} \\ I_{\max,h,b} & \text{for } I'_{M,h}(\zeta) \geq I_{\max,h,b} \end{cases} \quad (9)$$

with

$$I'_{M,h}(\zeta) = I_{0,h,b} + A_{h,b} \cdot e^{-\left(\frac{|\zeta-\mu_{h,b}|}{w_{h,b}}\right)^2},$$

respectively. The model function is a limited Gaussian function with an offset  $I_0$ , an amplitude  $A$ , a width  $w$ , a peak position  $\mu$  and an intensity limit  $I_{\max}$ . The index  $v$  refers to a vertical stripe and the index  $h$  to a horizontal stripe. By approximating the parameters, the determined peak position  $\mu_{v,a}$  serves as  $\xi$ -stripe location for a vertical stripe  $a$  and the determined peak position  $\mu_{h,b}$  is the  $\zeta$ -stripe location of a horizontal stripe  $b$ .

To calculate the absolute shadow position, the index of one grid in the image is needed. The locations of stripes in adjacent grids are used to determine the borders of each code bit. The intensity averaged in the quadratic range of each bit of the coded line is compared to an empirical threshold, that adapts to the image intensity. Mean bit intensities higher than the threshold are associated with a '0' and lower intensities provide a '1', and thus, the index is composed of the code bits.

The determined index enables to calculate the shadow position of the mask center. Indeed, using the index, each stripe in the image can be associated with a stripe in the mask

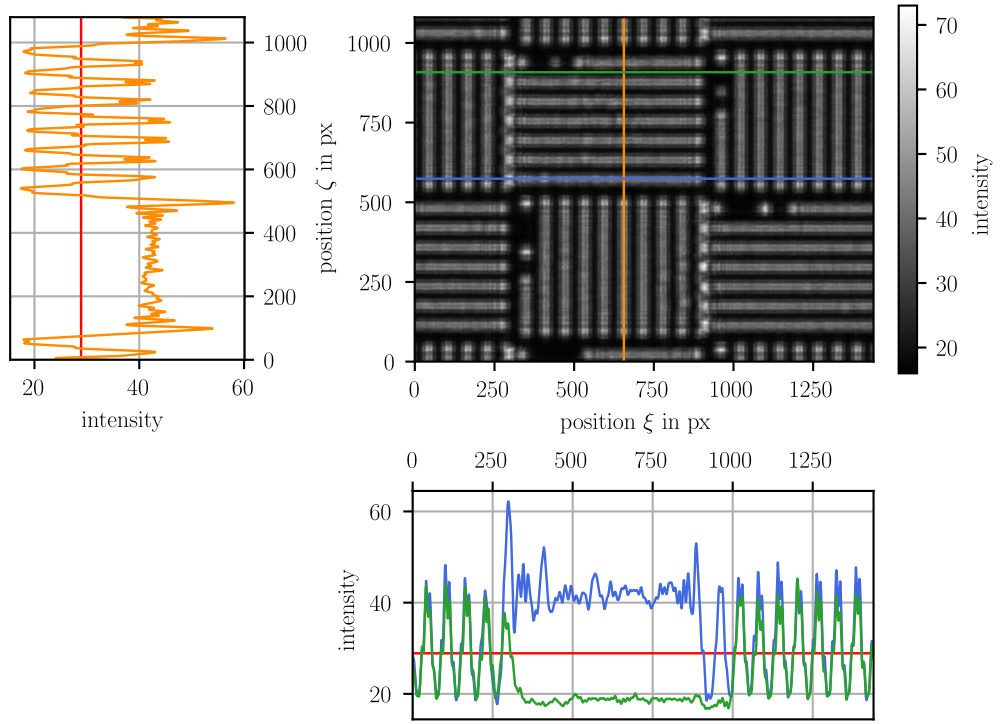


**Figure 5.** Camera image with intensity profiles used for grid segmentation. The lines in the image are the columns or rows where the filtered intensity profiles shown in the same color are taken. The red line in each intensity graph presents the threshold intensity. The intersections of the orange intensity profile and the threshold next to high-level-plateaus are horizontal borders. The left vertical border is located where the green intensity profile crosses the threshold on the left of the low-level-plateau and the right vertical border is located where the blue intensity profile crosses the threshold on the right of the high-level-plateau.

whose absolute position with respect to the mask center is known. To transfer the mask stripe position with respect to the mask center to the image plane, the magnification

$$k = \frac{l_S}{l_M} \quad (10)$$

of the stripe spacing  $l_S$  in the shadow on the camera chip with respect to the stripe spacing  $l_M$  in the mask is applied. Therefore, the horizontal mask center shadow position

$$\xi_i = \frac{1}{s_{v,1} - s_{v,0} + 1} \cdot \sum_{a=s_{v,0}}^{s_{v,1}} (\mu_{v,a} + d_{v,a} \cdot k) \quad (11)$$

and the vertical mask center shadow position

$$\zeta_i = \frac{1}{s_{h,1} - s_{h,0} + 1} \cdot \sum_{b=s_{h,0}}^{s_{h,1}} (\mu_{h,b} + d_{h,b} \cdot k) \quad (12)$$

are calculated from the stripe shadow positions  $\mu_{v,a}$  of each vertical stripe  $a$  or  $\mu_{h,b}$  of each horizontal stripe  $b$  visible in the image, the positions  $d_{v,a}$  in horizontal direction or  $d_{h,b}$  in vertical direction of each stripe in the mask and the magnification  $k$ . Here,  $s_{v,0}$  is the first and  $s_{v,1}$  the last index of the vertical stripes in the image and  $s_{h,0}$  the first and  $s_{h,1}$  the last index of the horizontal stripes. This way, the absolute shadow position  $(\xi_i, \zeta_i)$  is evaluated for each image. The shadow position is then inserted into Eq. (4) to (7) to obtain

the direction vector  $r_{m,n}$  pointing from the sensor to the LED, and the measured directions to the LED from several sensors finally provide the sought LED position according to Eq. (2) and (3).

### 3.2. Experimental setup with three sensors

Sensor 2 and sensor 3 are arranged perpendicular to sensor 1 because it is expected that a lower sum of the squares of the position component uncertainties is achieved if the angle between two measured direction vectors is close to  $90^\circ$  and if the angle of view from the sensor to the LED is close to  $0^\circ$  [22]. Sensor 1 is subsequently investigated in an axial measurement range of 500 mm beginning at a minimal measuring distance of 300 mm. The investigated lateral measurement range is 300 mm in horizontal direction and 200 mm in vertical direction, each centered in front of the sensor. Sensor 2 serves as second sensor for triangulation in the closer half of the axial measurement range of sensor 1 and sensor 3 covers the farther half. The investigated measurement range is located at a distance of 400 mm in front of sensor 2 and sensor 3. The LED is oriented in an angle of  $45^\circ$  towards the negative  $x$ - and  $y$ -axis so that the LED illuminates all sensors.

During the experiment, the LED is moved step-wise by the coordinate measuring machine Leitz PMM-F 30.20.7, which simulates the forming tool in ISF and simultaneously serves as reference. At each position, ten images are recorded with an exposure time of 25 ms. Note that a flashing high power LED can be used in future to meet the required measurement duration of 1 ms. In the first step, the LED is moved to defined positions to calibrate the sensor parameters. By recording ten images, the random error is reduced by averaging and thus the accuracy of the calibration is improved. In the second step, the LED is moved to a set of positions to investigate the measurement uncertainty. Here, ten images per position are recorded to study systematic and random errors.

In the uncertainty investigation, the LED is moved along the paths shown in Fig. 6, which are arranged parallel to the global  $x$ -,  $y$ - and  $z$ -axis. Images are captured each 10 mm where the LED movement stops. Therefore, the uncertainty of the 3D position measurement by means of triangulation of two shadow imaging sensors can be evaluated in dependence of the LED location in a measurement volume of  $500 \text{ mm} \times 300 \text{ mm} \times 200 \text{ mm}$ , which is sufficient with respect to the application in a multi-sensor system in ISF.

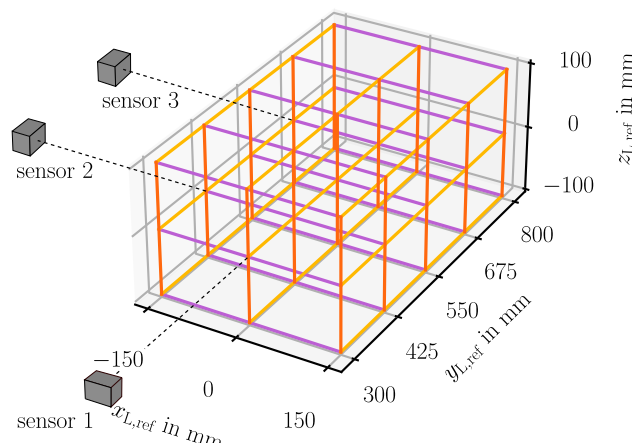


**Figure 6.** Paths on which the LED is moved in order to evaluate the 3D position measurement uncertainty. The lines are oriented parallel to the machine coordinate axes  $x$ ,  $y$  and  $z$ .

2. Devarajan, N.; Sivaswamy, G.; Bhattacharya, R.; Heck, D.P.; Siddiq, M.A. Complex incremental sheet forming using back die support on Aluminium 2024, 5083 and 7075 alloys. *Procedia Engineering* **2014**, *81*, 2298–2304. <https://doi.org/10.1016/j.proeng.2014.10.324>. 586  
587  
588
3. Ren, H.; Xie, J.; Liao, S.; Leem, D.; Ehmann, K.; Cao, J. In-situ springback compensation in incremental sheet forming. *CIRP Annals* **2019**, *68*, 317–320. <https://doi.org/10.1016/j.cirp.2019.04.042>. 589  
590
4. Konka, P.; Lingam, R.; Singh, U.A.; Shivaprasad, C.; Reddy, N.V. Enhancement of accuracy in double sided incremental forming by compensating tool path for machine tool errors. *The International Journal of Advanced Manufacturing Technology* **2020**, *111*, 1187–1199. <https://doi.org/10.1007/s00170-020-06149-1>. 591  
592  
593
5. Konka, P.; Lingam, R.; Reddy, N.V. Tool path design system to enhance accuracy during double sided incremental forming - An analytical model to predict compensations for small/large components. *Journal of Manufacturing Processes* **2020**, *58*, 510–523. 594  
595  
596
6. Sims-Waterhouse, D.; Isa, M.; Piano, S.; Leach, R. Uncertainty model for a traceable stereo-photogrammetry system. *Precision Engineering* **2020**, *63*, 1–9. <https://doi.org/10.1016/j.precisioneng.2019.12.008>. 597  
598  
599
7. Mutilba, U.; Yagüe-Fabra, J.A.; Gomez-Acedo, E.; Kortaberria, G.; Olarra, A. Integrated multilateration for machine tool automatic verification. *CIRP Annals* **2018**, *67*, 555–558. <https://doi.org/10.1016/j.cirp.2018.04.008>. 600  
601  
602
8. Sazonnikova, N.A.; Ilyuhin, V.N.; Surudin, S.V.; Svinarov, N.N. Increasing of the Industrial Robot Movement Accuracy at the Incremental Forming Process. In Proceedings of the 2020 International Conference on Dynamics and Vibroacoustics of Machines (DVM). IEEE, 2020, pp. 1–8. <https://doi.org/10.1109/DVM49764.2020.9243898>. 603  
604
9. Poozesh, P.; Sabato, A.; Sarrafi, A.; Niezrecki, C.; Avitabile, P.; Yarala, R. Multicamera measurement system to evaluate the dynamic response of utility-scale wind turbine blades. *Wind Energy* **2020**, *23*, 1619–1639. <https://doi.org/10.1002/we.2505>. 605  
606
10. Kumar, A.; Gulati, V.; Kumar, P. Investigation of process variables on forming forces in incremental sheet forming. *International Journal of Engineering and Technology* **2018**, *10*, 680–684. <https://doi.org/10.21817/ijet/2018/v10i3/181003021>. 607  
608  
609
11. Luhmann, T. Close range photogrammetry for industrial applications. *ISPRS Journal of Photogrammetry and Remote Sensing* **2010**, *65*, 558–569. <https://doi.org/10.1016/j.isprsjprs.2010.06.003>. 610  
611  
612
12. Gramola, M.; Bruce, P.J.K.; Santer, M. Photogrammetry for accurate model deformation measurement in a supersonic wind tunnel. *Experiments in Fluids* **2019**, *60*. <https://doi.org/10.1007/s00348-018-2652-7>. 613  
614  
615
13. Poozesh, P.; Baqersad, J.; Niezrecki, C.; Avitabile, P.; Harvey, E.; Yarala, R. Large-area photogrammetry based testing of wind turbine blades. *Mechanical Systems and Signal Processing* **2017**, *86*, 98–115. <https://doi.org/10.1016/j.ymssp.2016.07.021>. 616  
617  
618
14. Mendikute, A.; Yagüe-Fabra, J.A.; Zatarain, M.; Bertelsen, Á.; Leizea, I. Self-Calibrated In-Process Photogrammetry for Large Raw Part Measurement and Alignment before Machining. *Sensors (Basel, Switzerland)* **2017**, *17*. <https://doi.org/10.3390/s17092066>. 619  
620  
621
15. Shu, T.; Gharaaty, S.; Xie, W.; Joubair, A.; Bonev, I.A. Dynamic Path Tracking of Industrial Robots With High Accuracy Using Photogrammetry Sensor. *IEEE/ASME Transactions on Mechatronics* **2018**, *23*, 1159–1170. <https://doi.org/10.1109/TMECH.2018.2821600>. 622  
623  
624
16. Luo, P.F.; Chao, Y.J.; Sutton, M.A. Application of stereo vision to three-dimensional deformation analyses in fracture experiments. *Optical Engineering* **1994**, *33*, 981–990. 625  
626  
627
17. Fischer, J.D.; Woodside, M.R.; Gonzalez, M.M.; Lutes, N.A.; Bristow, D.A.; Landers, R.G. Iterative learning control of single point incremental sheet forming process using digital image correlation. *Procedia Manufacturing* **2019**, *34*, 940–949. <https://doi.org/10.1016/j.promfg.2019.06.108>. 628  
629  
630
18. Siebert, T.; Hack, E.; Lampeas, G.; Patterson, E.A.; Splitthof, K. Uncertainty Quantification for DIC Displacement Measurements in Industrial Environments. *Experimental Techniques* **2021**, *45*, 685–694. <https://doi.org/10.1007/s40799-021-00447-3>. 631  
632  
633
19. Tausendfreund, A.; Stöbener, D.; Fischer, A. In-Process Measurement of Three-Dimensional Deformations Based on Speckle Photography. *Applied Sciences* **2021**, *11*, 4981. <https://doi.org/10.3390/app11114981>. 634  
635  
636
20. Grenet, E.; Masa, P.; Franz, E.; Hasler, D. Measurement system of a light source in space. EP2593755, 2015. 637  
638  
639
21. Andre, A.N.; Sandoz, P.; Mauze, B.; Jacquot, M.; Laurent, G.J. Sensing one nanometer over ten centimeters: A microencoded target for visual in-plane position measurement. *IEEE/ASME Transactions on Mechatronics* **2020**, *25*, 1193–1201. <https://doi.org/10.1109/TMECH.2020.2965211>. 640  
641  
642
22. Dai, F.; Feng, Y.; Hough, R. Photogrammetric error sources and impacts on modeling and surveying in construction engineering applications. *Visualization in Engineering* **2014**, *2*. 643  
644  
645
23. Terlau, M.; von Freyberg, A.; Stöbener, D.; Fischer, A. In-Process Tool Deflection Measurement in Incremental Sheet Metal Forming. In Proceedings of the 2022 IEEE Sensors Applications Symposium (SAS). IEEE, 2022, pp. 1–6. <https://doi.org/10.1109/SAS54819.2022.9881345>. 646  
647  
648
24. Terlau, M.; von Freyberg, A.; Stöbener, D.; Fischer, A. In-Prozess-Messung der Werkzeugablenkung beim inkrementellen Blechumformen. In Proceedings of the 21. GMA/ITG-Fachtagung: Sensoren und Messsysteme 2022. VDE Verlag GmbH Berlin Offenbach, 2022, pp. 90–96. 649  
650  
651

**Disclaimer/Publisher's Note:** The statements, opinions and data contained in all publications are solely those of the individual author(s) and contributor(s) and not of MDPI and/or the editor(s). MDPI and/or the editor(s) disclaim responsibility for any injury to people or property resulting from any ideas, methods, instructions or products referred to in the content.